Error distribution in regional inversion of potential field data

R. Schachtschneider,[1,2] M. Holschneider[1] and M. Mandea[2]*

[1]*University of Potsdam, Germany. E-mail: rschacht@math.uni-potsdam.de*
[2]*Helmholtz Centre Potsdam - GFZ German Research Centre for Geosciences, Germany*

SUMMARY

An increasing number of regional inversions of gravity and magnetic field data have recently been computed, some based on satellite and ground data, some on satellite data only. In each case it is important to quantify the errors resulting from the confined data region or the satellite parameters. In this study we investigate the error distribution of regional inversions for scalar gravity and vector geomagnetic data from satellite data only. We include the effects of satellite altitude, size of the data region, signal-to-noise ratio and spherical harmonic degree of an *a priori* global field model. We evaluate our results on the basis of a regional inversion of the Earth's magnetic field.

Key words: Inverse theory; Satellite geodesy; Geopotential theory; Satellite magnetics.

1 INTRODUCTION

Since the satellite era the amount of available potential field data has increased tremendously and a huge variety of geomagnetic and gravity field models have been presented. Recent global models of the geoid derived from satellite data are, for example EIGEN-CHAMP03S (Reigber *et al.* 2004) from CHAMP data or EIGEN-GRACE02S (Reigber *et al.* 2005) and EIGEN-GRACE-GL04C (Förste *et al.* 2008) from GRACE and LAGEOS data. From these models regional features of the gravity field have been used to study mass changes over large river basins (Papa *et al.* 2008) or on continents (Schmidt *et al.* 2006), and also ice sheet melting over Greenland (Fleming *et al.* 2004) or Antarctica (Sagen *et al.* 2007). Recent global models of the magnetic field derived from satellite data only are, for example CHAOS (Olsen *et al.* 2006) and MF6 (Maus *et al.* 2008). When the magnetic field is modelled on a global scale, the determination of spherical harmonic coefficients tends to become unstable for higher degrees (Lesur *et al.* 2008). By regularization they may be determined up to degree 90 (Maus *et al.* 2006). Maus *et al.* (2008) were able to calculate a model up to spherical harmonic degree 120 by means of careful data selection, extensive correction, filtering and line levelling.

When investigating regional structures in great detail it is useful to concentrate the inversion on a bounded region. One of the important contributions in this field was done by Simons & Dahlen (2006). They show the connection of this problem to the Slepian's spaciospectral localization problem and expand the source field in a truncated Slepian function basis set.

Regional modelling allows to reduce the number of parameters in the inversion (Thébault *et al.* 2006) and to avoid problems of

inversion with globally supported basis functions (such as spherical harmonics). Thébault (2006) calculated a global magnetic field model from regional patches derived from satellite- and ground-based data. Regional gravity models have been presented, for example by Mayer-Gürr *et al.* (2006) and Schmidt *et al.* (2007). Ilk *et al.* (2007) stated that the heterogeneity of the gravity field cannot be taken into account by globally supported basis functions and thus modelled only long and medium wavelengths by spherical harmonics and refined that field locally using space localizing basis functions. Moreover, the polar gap, present in all satellite data sets, complicates global inversions. Simons & Dahlen (2006) have also solved the polar gap problem, providing a very efficient algorithm for this situation present in all satellite surveys.

It is the aim of this study to estimate the magnitude and distribution of errors arising from regional inversion of satellite data. The modelling errors are investigated depending on satellite altitude, size of the data region, magnitude of measurement noise and degree of an *a priori* global internal field model. The errors are then compared to results of existing regional inversions.

This paper starts with a short overview of the theoretical background of regional modelling in Section 2. Section 3 deals with the error distribution of global data coverage to demonstrate two fundamental error sources in data inversion. Section 4 describes the data used for the numerical experiments, and in the following section the results are presented and discussed.

2 THEORETICAL BACKGROUND

2.1 General considerations

In regional inversion we need to consider the interplay of three ingredients. On the one hand, there is the bounded modelling region on the Earth's surface where the potential field has to be computed.

---

*Now at: Université Paris Diderot - Institut de Physique du Globe de Paris Géophysique spatiale et planétaire, France.

On the other hand, we need to consider the data region, based on which the regional inversion is computed. In addition, we need to take into account a global model as prior information for the regional inversion. In the following all field contributions are assumed to be of internal origin.

In this paper we work in a Bayesian framework. The prior information about the potential field, Φ, is as follows. We first suppose that Φ is a potential field exterior to a sphere $\Omega = \{x^2 + y^2 + z^2 = R^2\}$ that contains all sources of the potential, so Φ is harmonic:

$$\Delta\Phi = 0 \quad \text{in} \quad \text{ext}\,\Omega,$$

where $\Delta = \nabla^2$ denotes the Laplacian. We further assume that there is a bounded quadratic form, a generalized energy, Q such that

$$Q(\Phi) < \infty.$$

In the terminology of spline modelling, this can be seen as an *a priori* smoothness assumption about Φ. In Bayesian inversion, Q is related to the prior probability of the field through

$$\mathbb{P}(\Phi) \simeq \exp(-Q(\Phi)).$$

The second piece of prior information assumes that an *a priori* global internal field Φ_0 is perfectly known. The whole field can then be written as

$$\Phi = \Phi_0 + \Phi_1, \tag{1}$$

with Φ_1 being Q-orthogonal to Φ_0:

$$Q(\Phi_0, \Phi_1) = 0.$$

As a consequence we can write

$$Q(\Phi) = Q(\Phi_0) + Q(\Phi_1). \tag{2}$$

The *a priori* model is improved through measurements. Supposing the field is known at the radius, R, of the sphere Ω, the potential at a point $\mathbf{x}$ at altitude h is given by Freeden & Michel (2004)

$$u(\mathbf{x}) = \int_\Omega P(\mathbf{x}, \xi)\,\Phi(\xi)\,\mathrm{d}\Omega, \tag{3}$$

where

$$P(\mathbf{x}, \xi) = \frac{1}{4\pi}\, \frac{R((R+h)^2 - R^2)}{(R^2 + (R+h)^2 - 2R(R+h)\cos\gamma)^{\frac{3}{2}}} \tag{4}$$

is the Poisson kernel with γ the angle between $\mathbf{x}$ and ξ, and Φ the potential just above the surface of the sphere Ω. Fig. 1 shows Poisson kernels for different satellite altitudes. The lower a satellite is the higher and narrower is the corresponding Poisson kernel. For $h \to 0$, the Poisson kernel tends to a Dirac delta function.

We now consider the case when the data are only known in a circular region D at altitude h (*cf.* Fig. 2). Satellite measurements at the altitude h can be described by

$$\Phi_h^\eta = K\Phi + \epsilon, \tag{5}$$

where ϵ is the noise of observations, modelled as Gaussian distributed noise with standard deviation η. The operator K is defined differently for the scalar and vector case and will be denoted K_s and K_v, respectively, if the distinction is important, and K if the equation demonstrates general facts that apply to both cases. In eq. (5), K is defined as $K_s = \chi_D P$ in the scalar case and $K_v = \chi_D \nabla P$ in the vector case, where χ_D is the characteristic function of the data region and $\nabla = (-\frac{\partial}{\partial\theta}\mathbf{e}_\theta, \frac{\partial}{\partial\phi}\mathbf{e}_\phi, -\frac{\partial}{\partial r}\mathbf{e}_\mathbf{r})$, so as to obtain vector data in the NEC-system (i.e. basis vectors pointing in the North, East and Centre direction). From eqs (1) and (5) follows

$$\Phi_h^\eta = K(\Phi_0 + \Phi_1) + \epsilon.$$

Because we assume the global model, Φ_0, to be perfectly known, we define a simulated measurement where the large scale *a priori* field contribution, Φ_0, is removed:

$$\tilde{\Phi}_h^\eta = \Phi_h^\eta - K\Phi_0 = K\Phi_1 + \epsilon. \tag{6}$$

Thus, the simulated measurements contain only small-scale field signals, Φ_1, and measurement noise. With the assumption about the noise, ϵ, follows that

$$\mathbb{E}(\epsilon) = 0, \quad \mathbb{E}(\epsilon(x)\epsilon(y)) = \eta^2\delta(x - y).$$
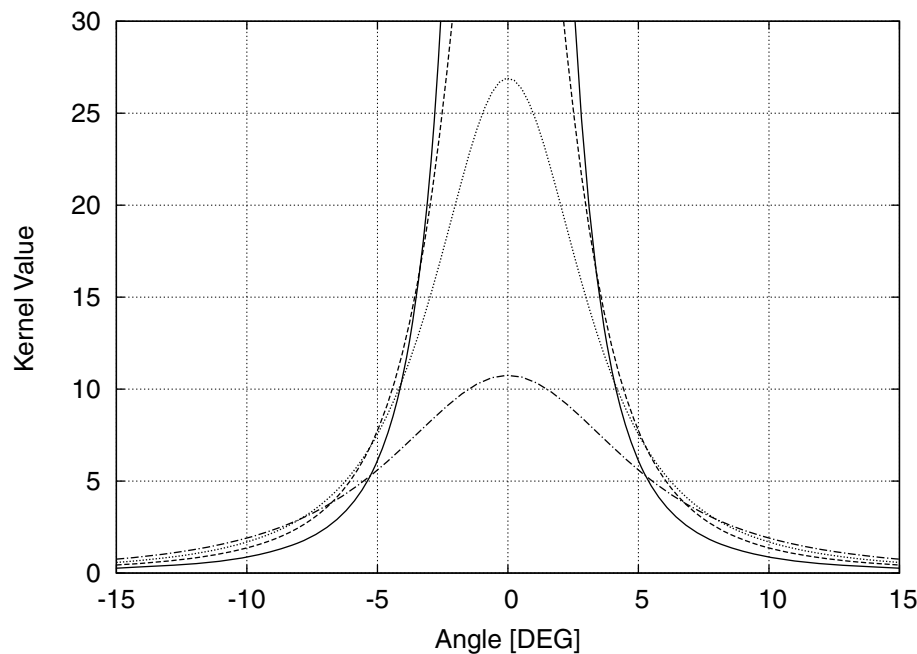

Figure 1. The Poisson kernel for different satellite altitudes (200 km—solid line, 350 km—dashed line, 500 km—dotted line, 800 km—dash-dotted line). Kernels of large satellite altitudes are broader than those of low altitude. Thus, for high altitudes, the contribution of distant sources to the value of the potential is greater than for small altitudes where the Poisson kernel is more localized.
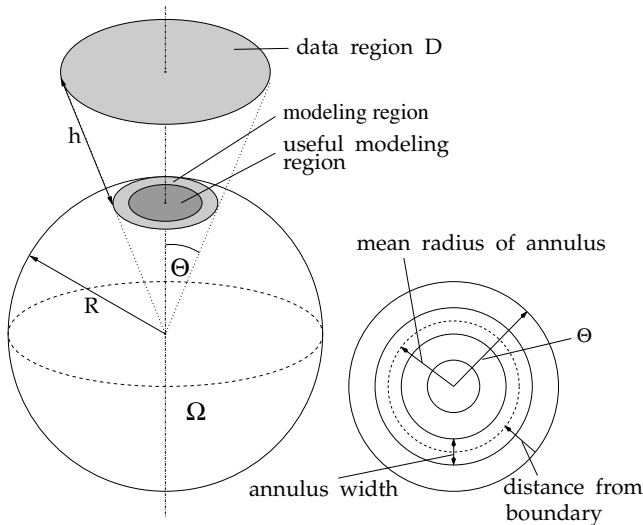
Figure 2. The potential field at the surface of the sphere Ω is assumed to be perfectly known. It is upward continued to the satellite altitude, h, and confined to a spherical cap (data region, D). In this region, the measurements are simulated. The simulated data are inverted in the modelling region and then compared to the original data. The dark grey region in the left figure is the part of the modelling region that is useful for modelling, that is where the errors do not exceed a certain level. The appropriate thickness of the light grey boundary region depending on modelling parameters is subject of this study. In the following, the error values will be calculated as RMS values in annuli around the cap centre and will associated to the mean annulus radius. This is depicted in the right part of the figure.

In principle, the operator K is invertible. Indeed, because $\tilde{\Phi}_h^0$ is a harmonic function, it is sufficient to know it in an arbitrary small neighbourhood of a given point. However, the inverse is unbounded and therefore in the presence of noise the inversion becomes unstable. The problem is ill posed. We thus need to regularize the reconstruction. One possibility of regularizing comes from spline modelling where the regularizing family of operators

$$L_\lambda = (K^{\mathrm{T}}K + \lambda Q)^{-1}K^{\mathrm{T}}$$

is considered. Q is the Q-energy operator in matrix notation. This leads to Tykhonov type of regularizing.

In this paper, an alternative regularizing family based on the singular value decomposition (SVD) of the operator K is considered:

$$K = \sum_{n=0}^{\infty} \sigma_n |U_n\rangle\langle V_n|, \tag{7}$$

with V_n and U_n column vectors of the matrices V and U. They form orthonormal bases in the domain and range of the operator K, respectively. The $\langle\cdot|$ and $|\cdot\rangle$ operators are the bra-ket operators as used in quantum mechanics (see, e.g. Dirac 1982). The σ_n are the corresponding singular values of K. We can suppose that the singular values are ordered such that

$$\sigma_n \geq \sigma_{n+1}.$$

We introduce the regularizing family for the inverse of K as

$$L_N = \sum_{n \leq N} \sigma_n^{-1} |V_n\rangle\langle U_n| \tag{8}$$

with N being a cut-off for the summation of weighted basis functions. This is the truncated SVD (TSVD) approach as described, for example, by Xu (1998). Let us note that in the continuous case this

is the truncated Slepian function approach described by Simons & Dahlen (2006). Because K is invertible all $\sigma_n \neq 0$ and the earlier expression is well defined. Clearly,

$$L_N K \Phi_1 \to \Phi_1 \quad \text{as} \quad N \to \infty, \tag{9}$$

so in case of noise free measurements, L_N can be used to approximate arbitrarily well the field Φ_1 on the Earth's surface from the regional simulated measurements $K\Phi_1$. If the measurements are contaminated by noise, an optimal working point, N_{opt}, has to be chosen. The optimality is based on a cost function d that measures the quality of the reconstruction.

Let $\tilde{\Phi}_N = L_N \tilde{\Phi}_h^\eta$ be the inverted potential field at the surface of Ω. We can use the distance measure definition

$$d(\Phi_1, \tilde{\Phi}_N)_D = ||\Phi_1 - \tilde{\Phi}_N||,$$

$$\text{where } ||\tilde{\Phi}||^2 = \int_D |\tilde{\Phi}|^2 \mathrm{d}\Omega \quad \text{(mean squared error)}, \tag{10}$$

for the average quality of the approximation in the region D and define

$$d(\Phi_1, \tilde{\Phi}_N)_{\mathbf{x}} = |\Phi_1(\mathbf{x}) - \tilde{\Phi}_N(\mathbf{x})|,$$

for the absolute error at a fixed point $\mathbf{x}$. Because d satisfies the triangle inequality, we can write

$$d(\Phi_1, \tilde{\Phi}_N)_D = d(\Phi_1, L_N K \Phi_1 + L_N \epsilon)_D$$
$$\leq d(\Phi_1, L_N K \Phi_1)_D + d(0, L_N \epsilon)_D. \tag{11}$$

There is a trade-off between the quality of approximation (as given by the first term) and the amplification of the noise (as given by the second term). For fixed prior information and fixed measurement geometry, the optimal choice for N depends on the noise level. It has to be determined such that the expected value of the cost function becomes minimal

$$N_{\mathrm{opt}} = \mathrm{argmin}\, \mathbb{E}\, d(\Phi_1, L_N(K\Phi_1 + \epsilon)). \tag{12}$$

The inequality (11) enables us to compute an upper bound for the error. The estimation variance (i.e. the expected variance of the amplified noise) at the location $\mathbf{x}$ can be calculated explicitly:

$$\mathrm{Var}(L_N \epsilon)(\mathbf{x}) = \sum_{n \leq N} \sigma_n^{-2} |V_n(\mathbf{x})|^2 \eta^2. \tag{13}$$

A second error, the bias or reconstruction error (i.e. the error due to the truncation of the inversion in eq. 8) has to be approximated through numerical tests. In the following these tests are described.

2.2 Setup and method

The inversion errors are evaluated in a frame shown in Fig. 2. We suppose the potential field is perfectly known at the surface of a sphere Ω with the radius R. The potential Φ_1 is then upward continued to satellite altitude h and confined to the data region (in the vector case the derivative is also calculated) using eq. (5). Then measurement noise is added.

Because our aim is to obtain predictions for the mean errors, we have performed Monte Carlo simulations consisting of the following steps:

(i) synthesis of global data according to Kaula's rule (scalar gravity data) or Mauersberger-Lowes spectrum (vector magnetic data) at the surface of Ω,

(ii) upward continuation of the potential data, calculation of the derivatives (vector data) and confinement to the data region,

(iii) addition of noise,

(iv) regional inversion,

(v) calculation of the residuals to the original data (scalar data) or their derivatives (vector data).

Then we calculate the RMS of the residuals within annuli around the cap centre to obtain a radial dependence of the expected inversion error.

3 ERROR ESTIMATION: TOWARDS THE OPTIMAL INVERSION CUT-OFF

For global data, the error computations can be carried out explicitly to some extent. This case is described in detail because the relevant error sources also appear in regional inversions, superposing effects due to the confined data region.

When inverting potential field data globally on a sphere there are two fundamental sources of error: amplification of noise or variance (e.g. measurement noise, unmodelled sources, etc.) and a reconstruction error due to the truncation of the basis functions series (bias). In the following, these two kinds of errors as well the influence of the number of measurements at satellite level are investigated and estimated.

3.1 Noise amplification (estimation variance)

A potential at the surface of a sphere is usually expressed as a truncation or filtering of an infinite series of weighted basis functions. A suitable family of functions are surface spherical harmonics (Freeden & Michel 2004). Let $\mathbf{r} = (r, \theta, \varphi)$, of length $||\mathbf{r}|| = r$, be a vector that describes the spatial position, and let $\hat{\mathbf{r}} = (\theta, \varphi)$, of length $||\hat{\mathbf{r}}|| = 1$, denote the positions of all points restricted to the unit sphere, Ω. The complete spherical harmonic representation of a (potential) field, Φ, has the form (Blakely 1995)

$$\Phi(\mathbf{r}) = R \sum_{l=0}^{\infty} \sum_{m=-l}^{l} \left(\frac{R}{r} \right)^{l+1} c_{l,m} Y_{l,m}(\hat{\mathbf{r}}), \tag{14}$$

where $Y_{l,m}$ are the surface spherical harmonics of degree l and order m and $c_{l,m}$ the corresponding weight factors or expansion coefficients. When R denotes the Earth's radius and $R + h$ the altitude of observation, we can thus write

$$\Phi(\mathbf{r}) = R \sum_{l=0}^{\infty} \sum_{m=-l}^{l} \left(\frac{R}{R+h} \right)^{l+1} c_{l,m} Y_{l,m}(\hat{\mathbf{r}}). \tag{15}$$

Let us now collect the spherical harmonic coefficients of the true potential at the Earth's surface in a singly indexed column vector

$$\mathbf{\Phi} = (\Phi_1, \ldots, \Phi_j, \ldots, \Phi_M)^{\mathrm{T}},$$

and the potential measured at satellite altitude in the column vector

$$\mathbf{\Phi}^h = \left(\Phi_1^h, \ldots, \Phi_i^h, \ldots, \Phi_N^h \right)^{\mathrm{T}},$$

where $\Phi_i^h = \Phi^h(\mathbf{r}_i)$ for a discrete set of points with $i = 1, \ldots, N$. The matrix operator mapping a set of spherical harmonics at Earth's surface to measurements at satellite altitude has the elements

$$K_{ij} = \left(\frac{R}{R+h} \right)^{l(j)+1} Y_{l(j),m(j)}(\hat{\mathbf{r}}_i). \tag{16}$$

It describes the contribution of the jth mode of the potential at Earth's surface to the ith field value at satellite altitude. The degree and order of the spherical harmonics are functions of the index j:

$$l(j) = \text{floor}(\sqrt{j-1}), \quad m(j) = j - l^2 - l - 1 \tag{17}$$

where floor (n) is the largest integer not greater than n. The least squares solution of the discretized problem (6) is

$$\mathbf{c}^{\text{est}} = (K^{\mathrm{T}} K)^{-1} K^{\mathrm{T}} \mathbf{d}, \tag{18}$$

where $\mathbf{d}$ is the vector of measurements at satellite altitude and $\mathbf{c}^{\text{est}}$ the vector with inverted spherical harmonic coefficients. In this expression

$$(K^{\mathrm{T}} K)_{jj'} = \left(\frac{R}{R+h} \right)^{l(j)+l'(j')+2} \sum_{i=1}^{N} Y_{l(j),m(j)}(\mathbf{r}_i) Y_{l'(j'),m'(j')}(\mathbf{r}_i).$$

Regarding the sum as a Riemann-sum it can be approximated by an integral:

$$(K^{\mathrm{T}} K)_{jj'} \approx \left(\frac{R}{R+h} \right)^{l(j)+l'(j')+2}$$

$$\times \frac{N}{4\pi R^2} \int_{\Omega_R} Y_{l(j),m(j)}(\mathbf{r}_i) Y_{l'(j'),m'(j')}(\mathbf{r}_i) \, d\Omega$$

and using the 4-π orthogonality of the spherical harmonics we obtain

$$= \left(\frac{R}{R+h} \right)^{2l+2} N \delta_{jj'}. \tag{19}$$

With this, the inverse of this matrix has the elements

$$(K^{\mathrm{T}} K)_{jj'}^{-1} \approx \left(\frac{R+h}{R} \right)^{2l(j)+2} \frac{\delta_{jj'}}{N}. \tag{20}$$

Inserting eq. (16) in the expression $K^{\mathrm{T}} \mathbf{d}$ and using eq. (20) the estimate for the jth spherical harmonic coefficient in eq. (18) becomes

$$c_j^{\text{est}} = \left(\frac{R+h}{R} \right)^{l+1} \frac{\delta_{jj'}}{N} \sum_{i=1}^{N} Y_{l,m}(\mathbf{r}_i) d(\mathbf{r}_i).$$

We will from now on exchange the vector subscript j with the subscripts for the degree and order, l and m, respectively. They are transformed with the relation (17). Writing now the measurements d_i as a sum of the true value and a measurement error this yields

$$c_{l,m}^{\text{est}} = \left(\frac{R+h}{R} \right)^{l+1} \frac{1}{N} \sum_{i=1}^{N} Y_{l,m}(\mathbf{r}_i) \, d_0(\mathbf{r}_i)$$

$$+ \left(\frac{R+h}{R} \right)^{l+1} \frac{1}{N} \sum_{i=1}^{N} Y_{l,m}(\mathbf{r}_i) \, \epsilon_i. \tag{21}$$

The first part is the reconstruction of the true spherical harmonic coefficient. The second part is the amplified noise. We are interested in the magnitude of the second part only. Recalling the rules for computing variances (Wilcox 2001):

$$\text{Var}(\alpha A + \beta B) = \alpha^2 \text{Var}(A) + \beta^2 \text{Var}(B),$$

if $\alpha, \beta \in \mathbb{R}$ and A and B are statistically independent random variables, its variance is

$$\text{Var}\left(c_{l,m}^{\text{err}}\right) = \left(\frac{R+h}{R} \right)^{2l+2} \frac{1}{N^2} \sum_{i=1}^{N} Y_{l,m}^2(\mathbf{r}_i) \, \text{Var}(\epsilon_i)$$

and approximating the sum by an integral it becomes

$$= \left(\frac{R+h}{R} \right)^{2l+2} \frac{1}{N^2} \frac{N}{4\pi(R+h)^2} \int_{\Omega_{R+h}} Y_{l,m}^2(\mathbf{r}) \eta^2 \, d\Omega$$

$$= \left(\frac{R+h}{R} \right)^{2l+2} \frac{\eta^2}{N} \tag{22}$$

As there are $2l + 1$ modes for the spherical harmonic degree l the variance per degree is

$$\text{Var}\left(c_l^{\text{err}}\right) = (2l + 1)\left(\frac{R + h}{R}\right)^{2l+2}\frac{\eta^2}{N}$$

and the total variance of the inverted noise is

$$E_1(M) = \text{Var}\left(c^{\text{err}}\right) = \frac{\eta^2}{N}\sum_{l=0}^{M}(2l + 1)\left(\frac{R + h}{R}\right)^{2l+2}. \tag{23}$$

Written as an integral this is approximately

$$E_1(M) \approx \frac{\eta^2}{N}\int_0^M (2l + 1)\left(\frac{R + h}{R}\right)^{2l+2}\,\mathrm{d}l. $$

3.2 Reconstruction error (bias)

In practice, a spherical harmonic series cannot be computed to infinity. The inversion has to be regularized, for example by filtering or truncation. When truncating the spherical harmonic field representation (*cf.* eq. 14) after degree M the remainder is

$$\bar{\Phi} = \sum_{l=M+1}^{\infty}\sum_{m=-l}^{l} c_{l,m}Y_{l,m}.$$

The total power of $\bar{\Phi}$ is

$$E_2(M) = \sum_{l=M+1}^{\infty} c_l^2,$$

where c_l is the total spectral power of degree l.

3.2.1 Gravity field

In case of the gravity field, using Kaula's rule of thumb (Kaula 1966), the gravity spectrum can be represented as in Fig. 3, and we can write

$$\frac{c_l}{\sqrt{2l + 1}} = \frac{C}{l^\gamma} \tag{24}$$

as a degree variance model. Then the total power can be written as

$$E_{2,G}(M) = \sum_{l=M+1}^{\infty}\frac{(2l + 1)\,C^2}{l^{2\gamma}}$$

with constants $C = 10^{-5}\ \text{m}^2\,\text{s}^{-2}$ and $\gamma = 2$ for geodesy. This sum can be regarded as a Riemann-sum and be approximated by the integral

$$E_{2,G}(M) = C^2\int_{M+1}^{\infty}\frac{2l + 1}{l^4}\,\mathrm{d}l.$$

Thus, for the gravity field the total error, depending on the truncation level M, can be written

$$E_G(M) = E_1(M) + E_{2,G}(M)$$

$$= \frac{\eta^2}{N}\int_0^M (2l + 1)\left(\frac{R + h}{R}\right)^{2l+2}\mathrm{d}l + C^2\int_{M+1}^{\infty}\frac{2l + 1}{l^4}\,\mathrm{d}l. \tag{25}$$

3.2.2 Magnetic field

For the magnetic field, the spectrum is different. Considering only the internal sources, two contributions, one from the core and one from the crust have to be taken into account (Fig. 3). The core field spectrum has, due to its deep source, a much steeper slope than the spectrum of the crustal field. Lowes (1974) approximated the power spectrum of the internal field by

$$c_l^2 = 4.0 \times 10^9(4.5)^{-l} + 150 \times \exp(-0.004\,l). \tag{26}$$

The total reconstruction error is then

$$E_{2,B}(M) = \sum_{l=M+1}^{\infty} 4.0 \times 10^9(4.5)^{-l} + 150 \times \exp(-0.004\,l), \tag{27}$$
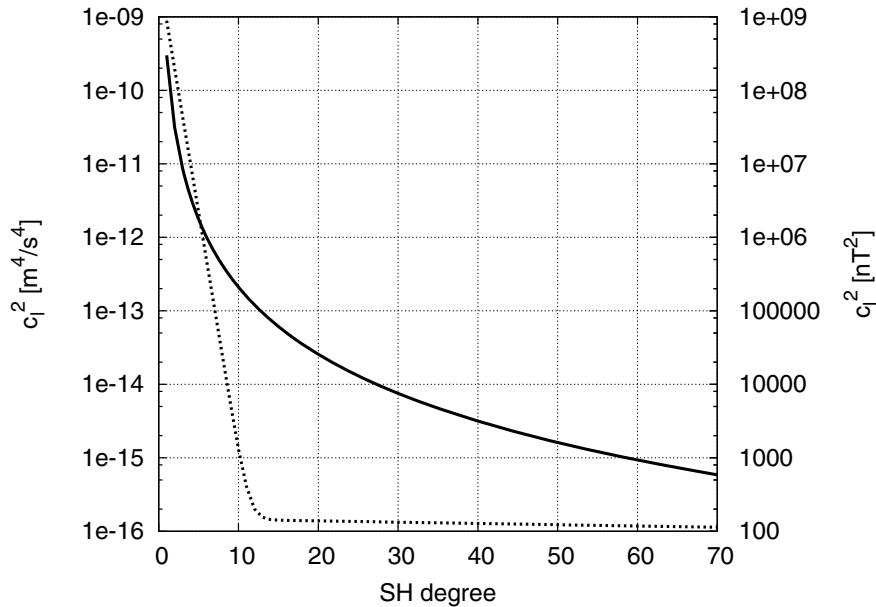

Figure 3. Kaula spectrum of gravity (solid line, and left scale) and Mauersberger-Lowes spectrum of the magnetic field (dotted line and right scale). The magnetic field spectrum has contributions from two sources: the steep part of the spectrum results from core contributions, the shallow part from crustal sources.
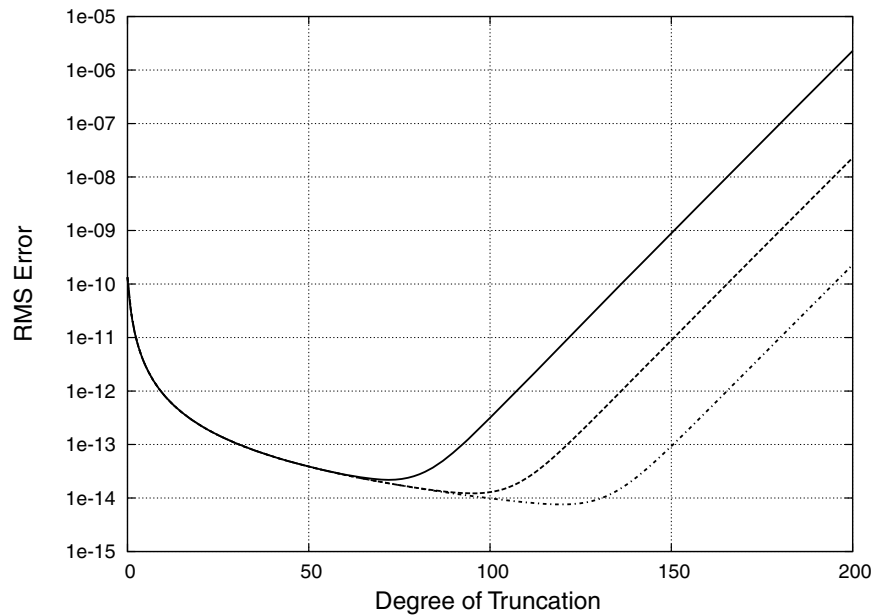
Figure 4. Inversion error for gravity field recovery for several noise levels. The inversion error is the sum of omission error (decreasing with increasing degree of the SH series) and commission error (increasing with increasing degree of the SH series). The minimum of this error is the optimal truncation point of the SH series with respect to the total error. Noise variance levels in this plot are 10^{-18} m^4 s^{-4} (solid line), 10^{-20} m^4 s^{-4} (dashed line) and 10^{-22} m^4 s^{-4} (dash-dotted line). The bin size is $2° \times 2°$. This is the bin size also used in the numerical experiments in Section 5.

yielding an inversion error of

$$E_B(M) = E_1(M) + E_{2,B}(M)$$
$$= \frac{\eta^2}{N} \int_0^M (2l+1) \left(\frac{R+h}{R} \right)^{2l+2} dl$$
$$+ \int_{M+1}^\infty 4.0 \times 10^9 (4.5)^{-l} + 150 \times \exp(-0.004\,l)\,dl.$$
(28)

The two error types have an antipodal dependence on the degree of signal reconstruction. The noise amplification grows exponentially with increasing degree of spherical harmonics whereas the reconstruction error decreases exponentially. The sum of these two errors has a minimum, which is the optimal truncation point for an inversion. For a given field type, the position of the optimal working point depends on the satellite altitude, the number of measurements and the noise amplitude. Fig. 4 shows an example of the inversion errors for a satellite altitude of 800 km and three different noise amplitudes. Indeed, the inversion error is indicated for the gravity field, with noise variance levels of 10^{-18} m^4 s^{-4}, 10^{-20} m^4 s^{-4} and 10^{-22} m^4 s^{-4}. For the large wavelength part (here up to SH degree 50), there are no differences in the evaluated RMS error. However, for SH degrees higher than 50, the amplified noise is the dominating error. For smaller noise levels, the minimum of the error curve is located at greater truncation degrees. Fig. 5 shows the position of the optimal working point (i.e. the inversion cut-off with minimal inversion error) depending on the bin size of the grid on which measurements are taken for three different noise levels in the scalar case.

3.3 Boundary effects in regional modelling

In addition to the errors mentioned earlier, edge effect errors have to be considered when the data base is not global. The Poisson kernel has, in general, a global support (*cf.* Fig. 1). As the degree of localization depends on the satellite altitude, with localization increasing

with decreasing altitude, the contribution of unmodelled sources from outside the data region increases with increasing satellite altitude. Fig. 6 shows the fraction of the Poisson kernel lying outside the data region—thus giving zero contribution in the inversion—depending on the distance to the boundary. It is the integral of the Poisson kernel over the complement of R divided by the integral of the Poisson kernel over the whole sphere:

$$f(\mathbf{x}) = \frac{\int_{\Omega \setminus R} P_h(\mathbf{x}, \xi)\,d\Omega}{\int_\Omega P_h(\mathbf{x}, \xi)\,d\Omega}.$$

Assuming a signal with energy equally distributed over the sphere this can be seen as the part of the signal that cannot be reconstructed in a regional inversion, however perfect the inversion scheme is.

4 DATA

4.1 Scalar potential data

When modelling the error distribution for the inversion of a scalar potential (e.g. the gravity potential), we start with synthetic data on a $2° \times 2°$ grid at the surface of the sphere Ω. The synthetic data are produced by a series of spherical harmonics from degree 15 to 70, the coefficients having zero mean and a standard deviation following the Kaula rule (*cf.* eq. 24). Using eq. (5), measurements at the satellite altitude are simulated.

With the SVD of the operator K_s it is possible to reconstruct a signal at the sphere Ω from the simulated measurements at satellite altitude (*cf.* eq. 9). For the scalar data approach, this yields a scalar potential at Ω which can be compared directly to the original data.

4.2 Magnetic field vector data

In planetary magnetism, the type of data to deal with are vector data, that is not the potential itself but the gradient of the potential:
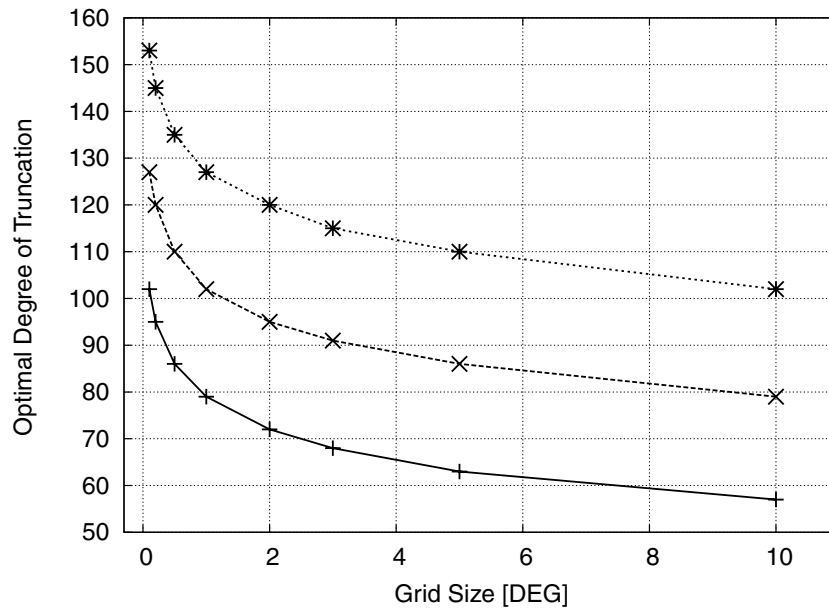
$$\mathbf{B} = -\nabla V,$$

Figure 5. Optimal truncation point depending on the bin size of the grid for three different noise levels in a global inversion of scalar data. The variance of the noise is 10^{-18} m^4 s^{-4}, 10^{-20} m^4 s^{-4} and 10^{-22} m^4 s^{-4} from bottom to top. The bin sizes of 10, 5, 3, 2, 1, 0.5, 0.2 and 0.1 degrees correspond to 648, 2592, 7200, 16 200, 64 800, 259 200, 1 620 000 and 25 920 000 data points, respectively.
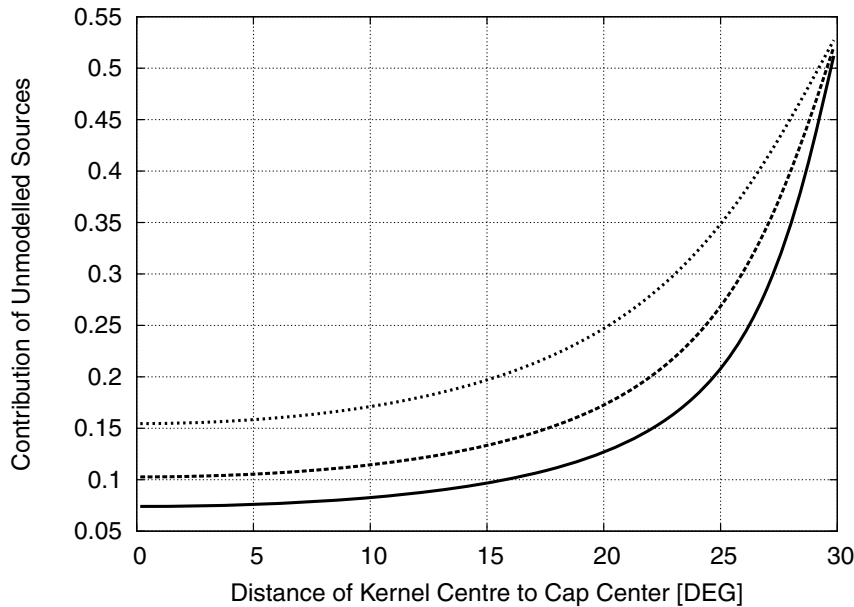

Figure 6. Ratio between the integral of the Poisson kernel over the complement of the data region and its integral over the whole sphere when the kernel is centred at some point inside the spherical cap. This represents the part of the contribution at a given location inside the cap that cannot be reconstructed because there are no data. This plot shows the dependency for satellite altitudes of 350 km (solid line), 500 km (dashed line) and 800 km (dotted line).

where V is the geomagnetic potential and **B** the magnetic flux density. Therefore, the procedure of estimating errors in magnetic field inversion differs from the procedure for gravity data inversion. In case of vector data we start with a set of spherical harmonic coefficients at the Earth's surface level that represent the potential (*cf.* eq. 14). The spherical harmonic coefficients have zero mean and a standard deviation according to the Mauersberger–Lowes spectrum (*cf.* eq. 26). The operator K_v that we want to analyse, maps the spherical harmonic coefficients to the gradient of the potential at satellite altitude restricted to the data region:

$$K_v : c_{l,m} \mapsto \chi_D(r) \left(\frac{R}{R+h} \right)^{l+1} c_{l,m} \nabla Y_{l,m}(\mathbf{r}).$$

Here χ_D is the characteristic function of the region D, where we take the measurements. Using eq. (9) it is possible to invert the synthetic data and obtain a set of new Gauss coefficients at the sphere surface. To estimate modelling errors, we compute the gradients of the geomagnetic potential given by the sets of synthetic and inverted Gauss coefficients and analyse the residuals.

In both cases, for scalar and vector data, it is necessary to solve eq. (12) to find the optimal working point, N_{opt}, for the operator L_N in eq. (9). To find that point we calculate the RMS error over the entire spherical cap after each inversion step. The optimal working point (where the error minimal) is reached when that RMS error reaches its minimum.

5 RESULTS

5.1 Error estimation

First, we have analysed the role of the *a priori* global model degree (*cf.* eq. 6) on the errors in regional modelling of scalar data. We have

considered modelling regions of varying size, from 10° to 30° radius and a fixed satellite altitude of 350 km. We have supposed internal field models up to degree 5, 10, 15 and 20. Although global models exist up to much higher degrees, it is only the first few coefficients, that are well constrained so that they can be considered to be well known. Because we want to analyse the incremental information gained by using data on regional scales, we can use these baseline models.

Fig. 7 shows, for fixed modelling region radius of 30°, the inversion error distribution, calculated as RMS error in annuli centred at the spherical cap centre. The error decreases with increasing global model degree, but the general shape of the residual distribution is similar in all cases. This is a superposition of two effects. One the
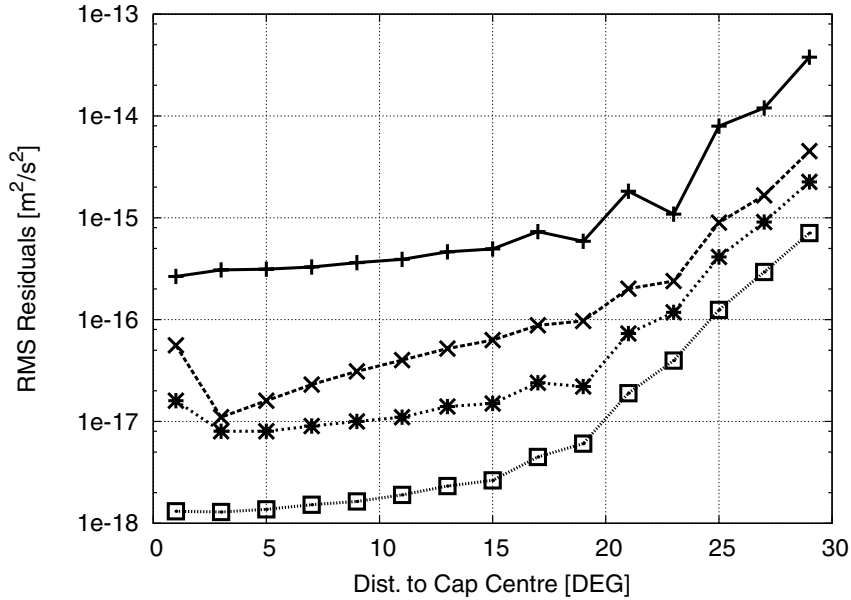

Figure 7. Inversion errors for different degrees of *a priori* known global models in gravity field recovery without noise. Global models are truncated at degree 5, 10, 15 and 20 (from top to bottom). The region radius is fixed at 30°. Each error value indicates the RMS residual computed in an annulus of 2° width centred at the spherical cap centre (*cf.* Fig. 2).
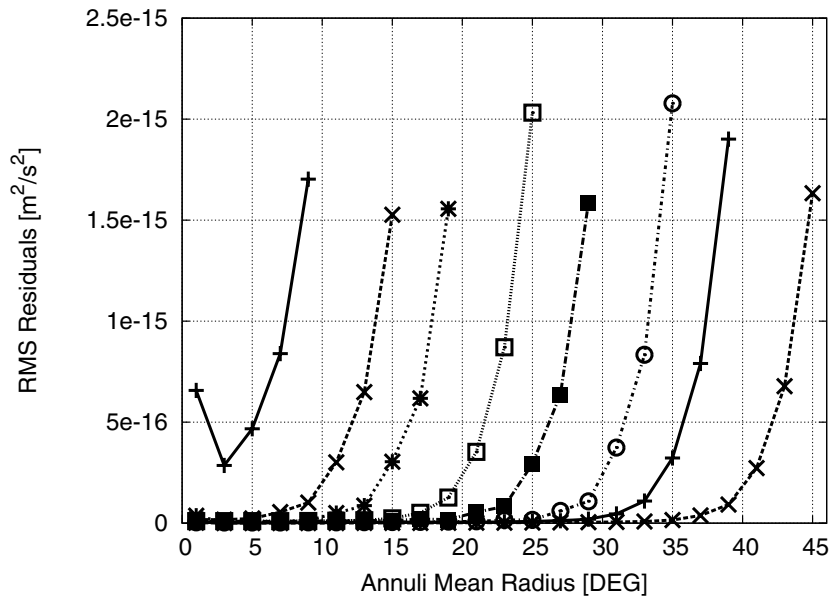

Figure 8. Inversion error for different data region radii for the scalar data case. Each curve corresponds to a given modelling region radius (10°, 16°, 20°, 26°, 30°, 36°, 40° and 46° from left to right). Global model is of spherical harmonic degree 15, the data are noise free.

one hand, wavelengths larger than the radius of the chosen modelling region cannot be sampled adequately and large inversion errors appear. Thus, excluding large wavelength data reduces the inversion error. On the other hand, the absolute contribution to the potential field decreases with increasing degree of the basis functions because the spherical harmonic coefficients follow the Kaula rule (*cf.* eq. 24) and Fig. 3 for the power spectrum of the synthetic data. Thus, the total amplitude of the synthetic signal decreases when considering higher degree global models and so does the inversion error.

The next test investigate the influence of the data region size. With fixed satellite altitude, degree of global model and noise level, the cap radius of the data region is varied between $10°$ and $35°$ for scalar data and between $10°$ and $45°$ for vector data. As shown in Figs 8 and 9, the error decays from the boundary of the modelling region towards the centre. It turns out that the thickness of the boundary region and the maximum error at the boundary are essentially independent of the modelling region radius, provided the region is larger than the longest wavelength present in the data.

It is interesting to zoom on the maximum error for each region radius. Fig. 10 shows the inversion errors at the cap boundary for different region radii with the same data spectrum (i.e. main field truncated at degree 15). With a data region large enough, the maximum error at the boundary saturates.

The boundary region could also be defined with respect to a desired accuracy that is to be reached in the remaining modelling region. In case of properly high-pass filtered data, the size of a boundary region defined this way does not change with data region size as can be seen in Fig. 11. It shows the inversion errors data regions with cap radii varying between $20°$ and $45°$. The global model truncation is degree 15 in all cases, the simulated data are noise free. The error values are printed depending on the distance of the annulus to the boundary (*cf.* Fig. 2).

On the other hand, the size of boundary region depends on the satellite altitude. Fig. 12 shows the modelling error for a fixed data region size of $30°$ radius and several satellite altitudes. The noise amplification increases with altitude (*cf.* eq. 22). For lower satellite altitudes, the inversion errors decrease more quickly from the cap boundary towards the centre. This is an effect of the shape of the Poisson kernel varying with altitude (*cf.* Fig. 1): it is narrower for lower altitudes and thus influences of distant sources on the potential at a certain point are smaller than for high satellite altitudes where the kernel is broader.

In a last series of tests, we are interested in the noise amplification distribution within the modelling region. With fixed data region size and satellite altitude, the variance of the noise added at the satellite level is varied. The variance of the Gaussian distributed noise varies between 0.1 and 5 nT for the vector data. Fig. 13 shows the error distribution for several noise levels. They all show the same characteristics and differ only in magnitude proportional to the noise level at satellite altitude.

5.2 Regional modelling

Another aim of this study is to compare the errors predicted in the tests to regional models of the magnetic field to estimate which of the features in the inversion are justified and which lie below the noise level. As, currently, there are no available regional magnetic field models based on satellite data only, we compute our own regional model of the magnetic anomaly field using the localized basis functions described by Lesur (2006). This approach is a predecessor of the harmonic splines used by Geese *et al.* (2010). The harmonics splines have also been used by Shure *et al.* (1982) in modelling the
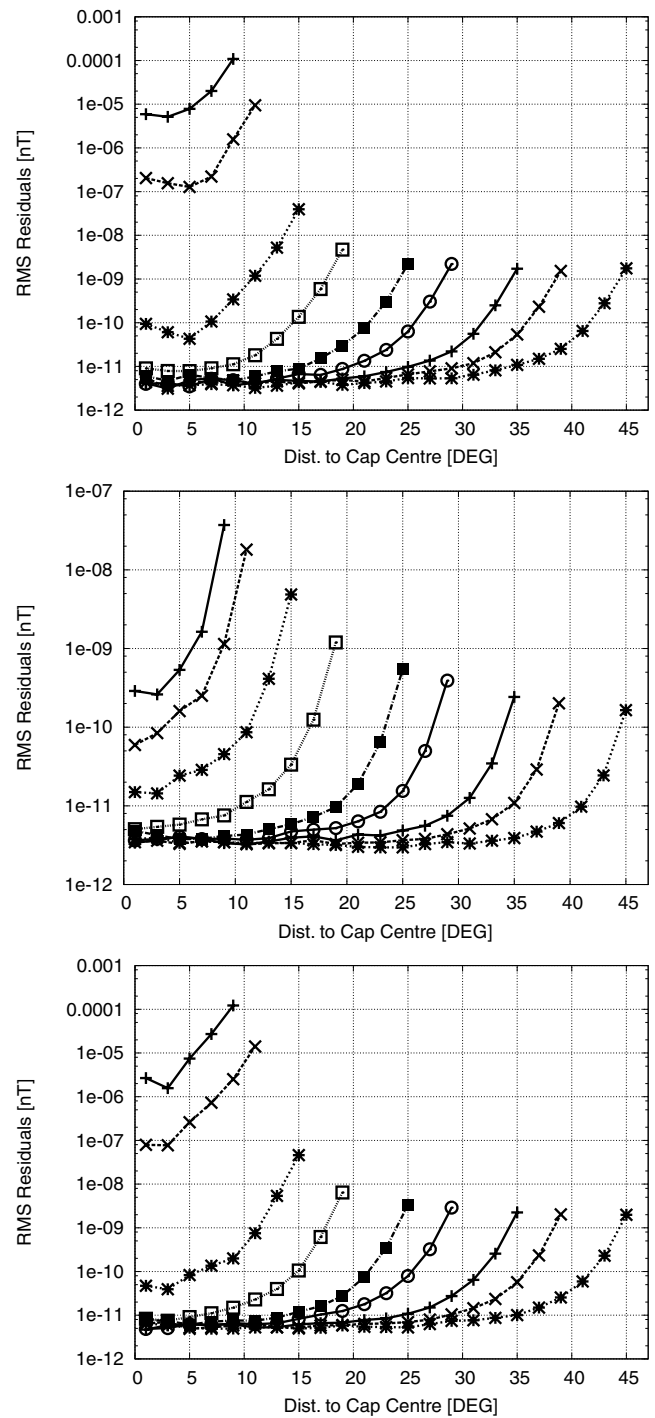

Figure 9. Inversion error for different data region radii for the noise free vector data case; top panel: X-component, middle panel: Y-component, bottom panel: Z-component of vector data. The residuals are RMS values over annuli around the cap centre, the modelling region radii vary between $10°$ and $45°$. Global model degree is 15.

geomagnetic field at global scale. As an example region we choose the Australian continent and invert satellite data in spherical cap of radius $20°$, centred at $130°E$, $20°S$. Prior to the inversion we remove an internal field model (GRIMM) of spherical harmonic degree 16.

After the model calculation, the regions where the absolute field values are smaller than the predicted error at the same location are eliminated from the maps. For error prediction we use the error
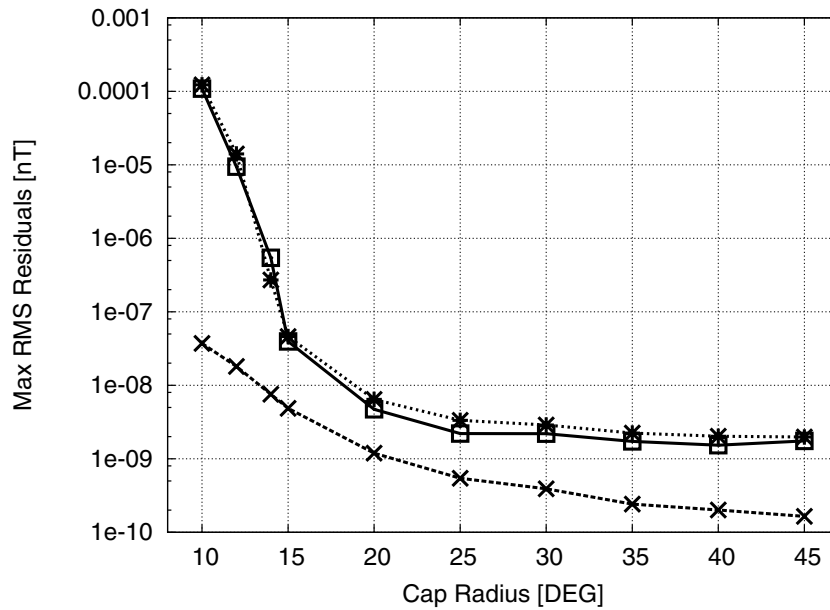
Figure 10. Maximum error at the boundary for different data region radii for the noise free vector data case (solid line: X- component, dashed line: Y-component, dotted line: Z-component). Global model degree is 15, corresponding to a wavelength of about 23°. A saturation of the error is reached in case of the X and Z components at a radius of about the order of the largest wavelength. For the Y-component there is no visible saturation.
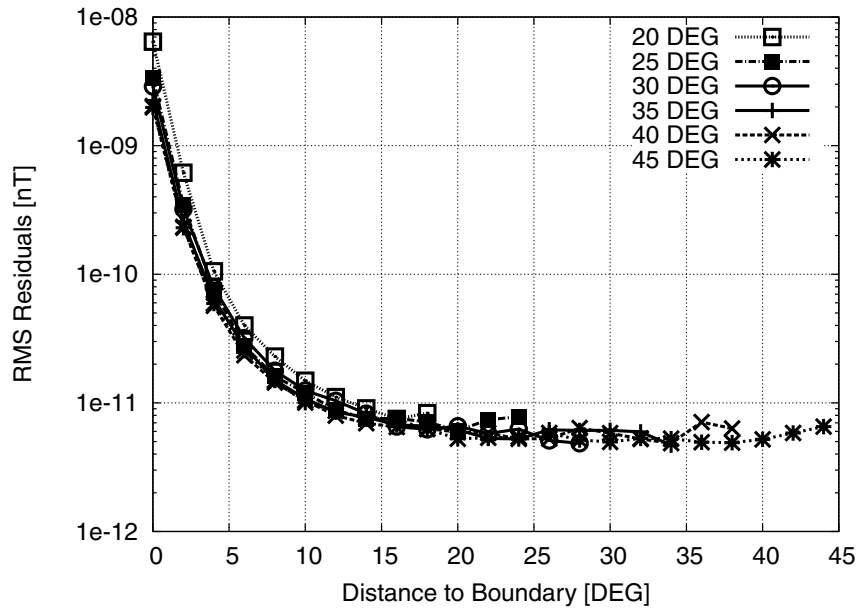

Figure 11. RMS error of the Z-component data (noise free) as a function of the distance from the data region boundary for different region radii. The maximum errors at the boundary are of the same magnitude, the error decrease towards the centre is similar for all curves.

profiles calculated earlier in this study for satellites with 500 km altitude and 5 nT noise level. Features with absolute field values larger than the error prediction are significant, those with smaller absolute values are indistinguishable from amplified noise. Fig. 14 shows the comparison of maps for the three field components before and after removing the features with low magnitude. It reveals that all the major features of the inversion have significant amplitudes. Only minor parts near the boundary are cut out or the shape of some features is not surely determined. In the central region, the removed parts are basically the transitions between regions with opposite signs. This indicates whether there is great uncertainty in the shape of the features (small transition zone) or not (broad transition zone).

6 DISCUSSION AND CONCLUSIONS

In this study, we have investigated the role of several parameters on errors in regional inversion of potential fields, such as satellite altitude, size of the data region, noise level, and degree of an *a priori* internal field model. There are several types of errors in potential field inversion, each depending on a different parameter or a combination of them. The error types are noise amplification, reconstruction errors and edge effects due to the localized data base. The reconstruction error does not depend on the investigated parameters but only on the truncation point in the signal reconstruction. The amplified noise in the inverted field is influenced by the
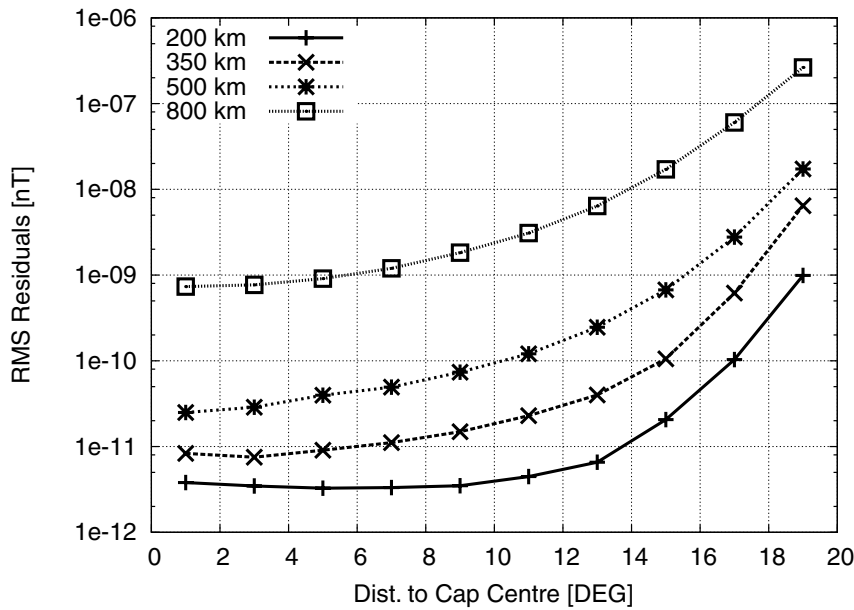
Figure 12. Dependence of inversion error on satellite altitude. The size of the data region is 20°, the data are noise free. For higher altitudes the general error level is higher (due to a stronger noise amplification) and the error decay from the boundary towards the centre is slower than for low altitudes. The latter is due to the loss of localization of the Poisson kernel with increasing altitudes (*cf.* Fig. 1).
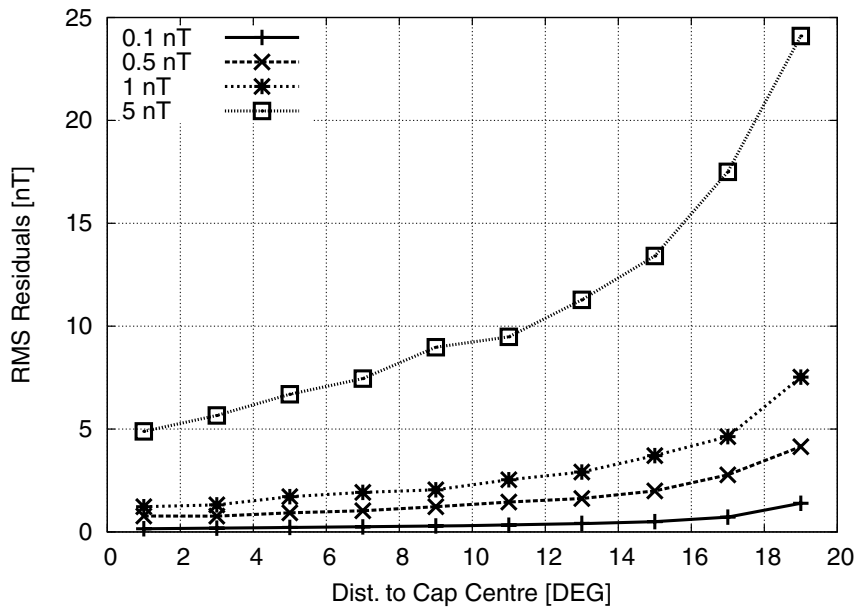

Figure 13. Dependence of inversion error on noise level in the vector data case. The size of the data region is 20°, satellite altitude is 350 km. Plotted here is the Z-component, the behaviour for the X and Y components is similar.

measurement noise level and the satellite altitude. The latter is also the main influencing factor for error at the boundary and its decaying behaviour towards the centre of the model region. The internal field model degree is only important in choosing its value such that the longest wavelength in the data is not larger than the model region radius.

The general shape of the residual distribution over the modelling region is equal for all numerical tests throughout this study. It shows smallest residuals in the central region and an exponential like growth towards the boundaries. The investigated parameters influence the residual level and the steepness of the curve towards the boundaries.

The degree of an *a priori* internal field model is important for the analysis of errors because it determines the largest wavelength present in the available data. This wavelength must be smaller than the radius of the data region to be able to properly represent the field within the confined region. Larger wavelengths are not well restrained and result in high inversion errors.

The satellite altitude influences the error amplitude and the steepness of the radial dependence, especially near the cap boundaries. For greater satellite altitudes, noise is amplified more strongly and the error curve is shifted upwards. Secondly, with increasing satellite altitude the Poisson kernel becomes broader and thus the dependence of an inverted value on data values outside the data
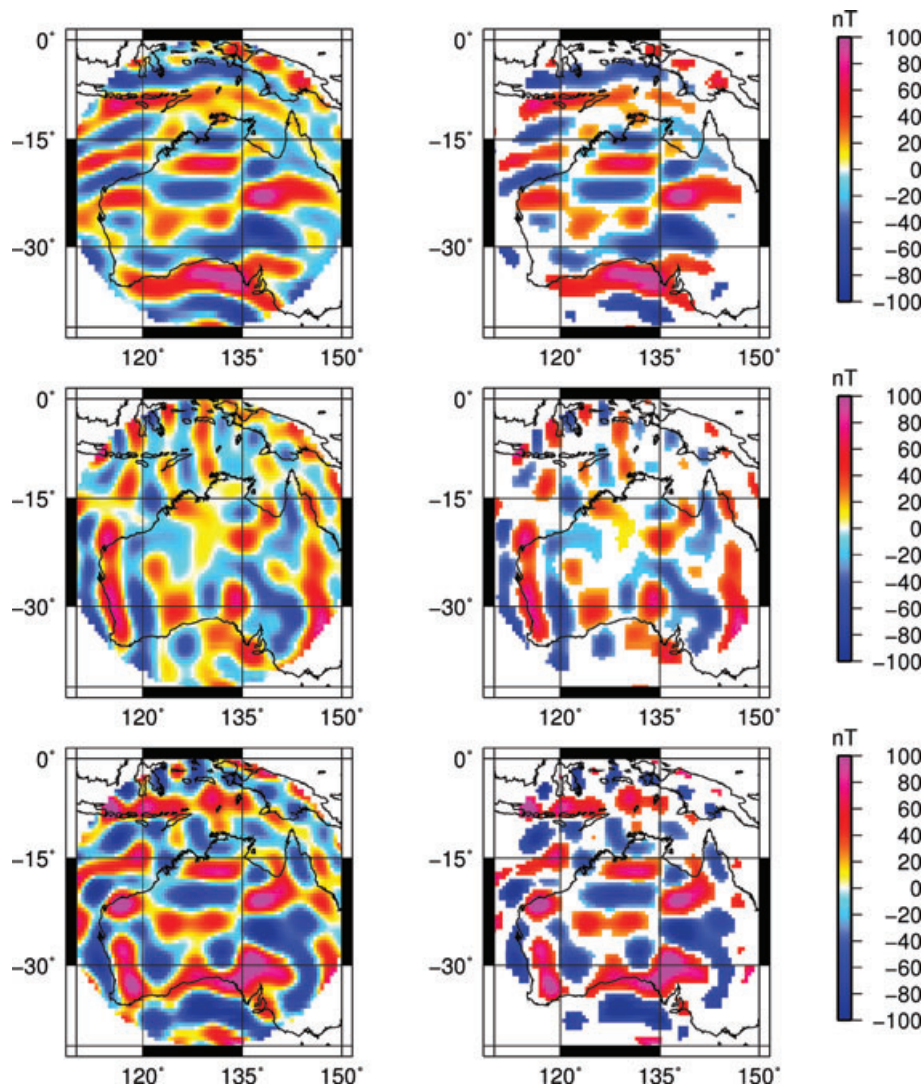
Figure 14. Regional inversion of the magnetic anomaly field over Australia: North, East and Centre components from top to bottom. The left panels show the raw inversion over the full data region. The right panels show the remaining features after removing those with a magnitude below the noise level. The used error prediction curve has the following parameters: satellite altitude: 500 km, noise level: 5 nT. Near the edges there are minor features with amplitudes smaller than the noise level or where their shape is only poorly determined.

region increases. Because there is no information about the field outside the data region, the error increases with increasing satellite altitude.

The noise level at satellite altitude influences the error amplitudes. The general shape of the error curves is not changed for different noise levels. They are shifted upwards towards greater errors for greater noise amplitudes. When investigating the dependence on the data region radius it turned out that the error decay from the boundary towards the centre of the data region is similar for different radii, provided the radii are greater than the minimum wavelength in the used data. Thus, the width of the boundary region needed to achieve a certain accuracy in the modelling region does not depend on the data region radius.

The regional inversion calculated in order to verify whether or not the inverted features are significant, i.e. larger than the expected error at that location, revealed that most of the prominent features lie above the noise level. Nevertheless near the boundaries there are parts of the inverted field that have smaller amplitudes than the

amplified noise or are at least not well constrained in their shape. Thus they must be removed from the eventual inversion by the choice of a suitable boundary region. Here we used satellite data only, so when ground based data are also used in an inversion the accuracy should increase and features existing in the data should be better described. The results of this study could be very beneficial in regional inversions of gravity data provided by the newly launched GOCE mission or of magnetic data expected from the future Swarm mission.

REFERENCES

Blakely, R.J., 1995. *Potential Theory in Gravity and Magnetic Applications,* Cambridge University Press, Cambridge.

Dirac, P., 1982. *The Principles of Quantum Mechanics,* 4th edn, Oxford University Press, Oxford.

Fleming, K., Martinec, Z. & Hagedorn, J., 2004. Geoid displacement about Greenland resulting from past and present-day mass changes in the Greenland Ice Sheet, *Geophys. Res. Lett.,* **31,** L06617, doi:10.1029/2004GL019469.

Förste, C. *et al.*, 2008. The GeoForschungsZentrum Potsdam/Groupe de Recherche de Geodesie Spatiale satellite-only and combined gravity field models: EIGEN-GL04S1 and EIGEN-GL04C, *J. Geodesy,* **82**(6), 331–346, doi:10.1007/s00190-007-0183-8.

Freeden, W. & Michel, V., 2004. *Multiscale Potential Theory (With Applications to Geo-science),* Birkhäuser, Boston, Basel, Berlin.

Geese, A., Hayn, M., Mandea, M. & Lesur, V., 2010. Regional Modelling of the Southern African Geomagnetic Field using Harmonic Splines, *Geophys. J. Int.,* in press (doi:10.1111/j.1365-246X.2010.04575.x).

Ilk, K., Eicker, A. & Mayer-Gürr, T., 2007. Global gravity field recovery by merging regional focusing patches: an integrated approach, in *Dynamic Planet: Monitoring and Understanding a Dynamic Planet with Geodetic and Oceanographic Tools,* Vol. 130, Proceedings of IAG Symposium on Dynamic Planet, Cairns, Australia.

Kaula, W.M., 1966. Global harmonic and statistical analysis of gravity, in *Extension of Gravity Anomalies to Unsurveyed Areas,* Vol. 9, pp. 58–67. ed. Orlin, H., American Geophysical Union Monograph.

Lesur, V., 2006. Introducing localized constraints in global geomagnetic field modelling, *Earth Planets Space,* **58,** 477–483.

Lesur, V., Wardinski, I., Martin, R. & Mioara, M., 2008. GRIMM: the GFZ Reference Internal Magnetic Model based on vector satellite and observatory data, *Geophys. J. Int.,* **173,** 382–394, doi:10.1111/j.1365-246X.2008.03724.x.

Lowes, F.J., 1974. Spatial power spectrum of the main geomagnetic field, and extrapolation to the core, *Geophys. J. R. astr. Soc.,* **36,** 717–730.

Maus, S., Rother, M., Hemant, K., Stolle, C., Lühr, H., Kuvshinov, A. & Olsen, N., 2006. Earth's lithosperic magnetic field determined to spherical harmonic degree 90 from CHAMP satellite measurements, *Geophys. J. Int.,* **164,** 319–330.

Maus, S. *et al.*, 2008. Resolution of direction of oceanic magnetic lineations by the sixth-generation lithospheric magnetic field model from CHAMP satellite magnetic measurements, *Geochem. Geophys. Geosyst.,* **9**(7), Q07021, doi:10.1029/2008GC001949.

Mayer-Gürr, T., Eicker, A. & Ilk, K.H., 2006. Gravity field recovery from GRACE-SST data of short arcs, in *Observation of the Earth System from Space,* pp. 131–148, eds Flury, J., Rummel, R., Reigber, C., Rothacher, M., Boedecker, G. & Schreiber, U., Springer, Berlin.

Olsen, N., Lühr, H., Sabaka, T.J., Mandea, M., Rother, M., Tffner-Clausen, L. & Choi, S., 2006. CHAOS—a model of the earth's magnetic field derived from CHAMP, ørsted, and SAC-C magnetic satellite data, *Geophys. J. Int.,* **166**(1), 67–75, doi:10.1111/j.1365-246X.2006.02959.x.

Papa, F., Güntner, A., Frappart, F., Prigent, C. & Rossow, W.B., 2008. Variations of surface water extent and water storage in large river basins: a comparison of different global data sources, *Geophys. Res. Lett.,* **35,** L11401, doi:10.1029/2008GL033857.

Reigber, C. *et al.*, 2004. Earth Gravity Field and Seasonal Variability from CHAMP, in *Earth Observation with CHAMP—Results from Three Years in Orbit,* pp. 25–30, eds Reigber, C., Lühr, H., Schwintzer, P. & Wickert, J., Springer, Berlin.

Reigber, C., Schmidt, R., Flechtner, F., König, R., Meyer, U., Neumayer, K.-H., Schwintzer, P. & Yuan Zhu, S., 2005. An Earth gravity field model complete to degree and order 150 from GRACE: EIGEN-GRACE02S, *J. Geodyn.,* **39**(1), 1–10.

Sagen, I., Martinec, Z. & Fleming, K., 2007. Regional ice-mass changes and glacial-isostatic adjustment in Antarctica from GRACE, *Earth planet. Sci. Lett.,* **264,** 291–401.

Schmidt, R. *et al.*, 2006. GRACE observations of changes in continental water storage, *Glob. planet. Change,* **50,** 112–126.

Schmidt, M., Fengler, M., Mayer-Gürr, T., Eicker, A., Kusche, J., Sanchez, L. & Han, S.-C., 2007. Regional gravity modeling in terms of spherical base functions, *J. Geodesy,* **81,** 17–38, doi:10.1007/s00190-006-0101-5.

Shure, L., Parker, R.L. & Backus, G.E., 1982. Harmonic splines for geomagnetic modelling, *Phys. Earth planet. Inter.,* **28**(3), 215–229.

Simons, F.J. & Dahlen, F.A., 2006. Spherical Slepian functions and the polar gap in geodesy, *Geophys. J. Int.,* **166,** 1039–1061.

Thébault, E., 2006. Global lithospheric magnetic field modelling by successive regional analysis, *Earth Planets Space,* **58,** 485–495.

Thébault, E., Schott, J.J. & Mandea, M., 2006. Revised spherical cap harmonic analysis (R-SCHA): validation and properties, *J. geophys. Res.,* **111,** B01102, doi:10.1029/2005JB003836.

Wilcox, R.R., 2001. *Fundamentals of Modern Statistical Methods,* Springer Verlag, New York.

Xu, P., 1998. Truncated SVD methods for discrete linear ill-posed problems, *Geophys. J. Int.,* **135**(2), 505–514, doi:10.1046/j.1365-246X.1998.00652.x.